



저작자표시-비영리-변경금지 2.0 대한민국

이용자는 아래의 조건을 따르는 경우에 한하여 자유롭게

- 이 저작물을 복제, 배포, 전송, 전시, 공연 및 방송할 수 있습니다.

다음과 같은 조건을 따라야 합니다:



저작자표시. 귀하는 원저작자를 표시하여야 합니다.



비영리. 귀하는 이 저작물을 영리 목적으로 이용할 수 없습니다.



변경금지. 귀하는 이 저작물을 개작, 변형 또는 가공할 수 없습니다.

- 귀하는, 이 저작물의 재이용이나 배포의 경우, 이 저작물에 적용된 이용허락조건을 명확하게 나타내어야 합니다.
- 저작권자로부터 별도의 허가를 받으면 이러한 조건들은 적용되지 않습니다.

저작권법에 따른 이용자의 권리는 위의 내용에 의하여 영향을 받지 않습니다.

이것은 [이용허락규약\(Legal Code\)](#)을 이해하기 쉽게 요약한 것입니다.

[Disclaimer](#)

공학석사학위논문

이중 오리피스에서 발생하는 두 합성 제트의 유동 상호작용에 관한 실험적 연구

**Experimental study on the flow interaction between
two synthetic jets emanating from a dual-orifice**

2020년 8월

서울대학교 대학원

기계공학부

김 무 성

이중 오리피스에서 발생하는 두 합성 제트의 유동 상호작용에 관한 실험적 연구

Experimental study on the flow interaction between two synthetic jets emanating from a dual-orifice

지도교수 황 원 태

이 논문을 공학석사 학위논문으로 제출함

2020년 4월

서울대학교 대학원

기계공학부

김 무 성

김무성의 공학석사 학위논문을 인준함

2020년 6월

위 원 장 : 최 해 천 (인)

부위원장 : 황 원 태 (인)

위 원 : 김 호 영 (인)

Abstract

Multiple orifice synthetic jet devices are becoming widely utilized for active flow control and jet impingement cooling, due to its mixing performance resulting from the vortices and jet interaction. Therefore, understanding the flow interaction between multiple synthetic jets is crucial in maximizing the potential for many industrial applications. In the present study, an experimental investigation on flow interaction between two synthetic jets generated from a dual-orifice device is performed. The influence of the orifice spacing ($s/D = 1.2, 2.0, \text{ and } 3.0$) and the dimensionless stroke length ($L_o/D = 13.7, 19.0, \text{ and } 28.3$) is analyzed at a fixed Reynolds number of $Re_o = 3700$. Phase-locked particle image velocimetry (PIV) is used to obtain time- and phase-averaged flow fields. The jet interaction is enhanced as the orifice spacing and the dimensionless stroke length decrease, resulting in shorter distances for the merging and combining points. In addition, the inner vortices between the two jets are deformed and cancelled due to the jet interaction, which leads to the inner and outer vortices merging into a single vortex. The vortex interactions and merging are delayed as the orifice spacing increases, while the advection speed of vortices is increased without change of flow structure as the dimensionless stroke length increases.

Keyword: Synthetic jet, Dual jets, Jet interaction, Phase-locked PIV, Vortex dynamics

Student Number: 2018 – 29172

Table of Contents

Abstract	i
Contents	ii
List of Figures	iii
List of Tables	vi
Nomenclature	vii
Chapter 1. Introduction.....	1
1.1 Research background	1
1.2 Purpose of research	3
Chapter 2. Experimental method.....	5
2.1 Experimental chamber and dual synthetic jet actuator.....	5
2.2 Phase-locked particle image velocimetry	6
2.3 Data reduction.....	7
Chapter 3. Time-averaged flow fields.....	12
3.1 Streamwise mean velocity distributions.....	12
3.2 TKE and PKE contours	15
Chapter 4. Phase-averaged flow fields.....	29
4.1 Phase-averaged vorticity contours.....	29
4.2 Vortex advection.....	30
Chapter 5. Conclusion.....	37
Bibliography	39
Abstract in Korean	41

List of Figures

FIGURE 1.1 Working principle of synthetic jet.....	4
FIGURE 2.1 Experimental setup.....	10
FIGURE 2.2 Dual orifice synthetic jet actuator.....	10
FIGURE 3.1 Schematic of dual jet configuration.....	17
FIGURE 3.2 Example of dual synthetic jet flow field ($s/D = 3.0$ & $L_o/D = 28.3$)	18
FIGURE 3.3 Time-averaged streamwise velocity contours with dimensionless stroke length $L_o/D = 28.3$, for (a) $s/D = 1.2$, (b) s/D $= 2.0$, and (c) $s/D = 3.0$	19
FIGURE 3.4 Time-averaged streamwise velocity contours with orifice spacing $s/D = 3.0$, for (a) $L_o/D = 13.7$, (b) $L_o/D = 19.0$, and (c) $L_o/D = 28.3$	20
FIGURE 3.5 Normalized streamwise velocities along the centerline (unfilled marker) and symmetry line (filled marker), for (a) fixed $L_o/D = 28.3$, and (b) fixed $s/D = 3.0$	21
FIGURE 3.6 (a) Streamwise locations of the merging points (unfilled marker) and the combining points (filled marker), (b) Extent of the	

merging region	23
FIGURE 3.7 Normalized streamwise velocity profiles in the region of $L_p < x < x_{cp}$, for $s/D = 3.0$ & $L_o/D = 28.3$	24
FIGURE 3.8 Outer half-velocity width and y' coordinate	25
FIGURE 3.9 Contours of turbulent kinetic energy (TKE) with the orifice spacing $s/D = 3.0$, for (a) $L_o/D = 13.7$, (b) $L_o/D = 19.0$, and (c) $L_o/D = 28.3$	26
FIGURE 3.10 Contours of phase-correlated kinetic energy (PKE) with the orifice spacing $s/D = 3.0$, for (a) $L_o/D = 13.7$, (b) $L_o/D = 19.0$, and (c) $L_o/D = 28.3$	27
FIGURE 3.11 Normalized PKE profiles in the region of $L_p < x < x_{cp}$, for $s/D = 3.0$ & $L_o/D = 28.3$	28
FIGURE 4.1 Phase-averaged vorticity contours for $s/D = 1.2$ and $L_o/D = 13.7$	32
FIGURE 4.2 Phase-averaged vorticity contours for $s/D = 1.2$ and $L_o/D = 28.3$	33
FIGURE 4.3 Phase-averaged vorticity contours for $s/D = 3.0$ and $L_o/D = 13.7$	34
FIGURE 4.4 Snapshots of $s/D = 1.2$, for (a) $L_o/D = 13.7$, (b) $L_o/D =$	

19.0, and (c) $L_0/D = 28.3$	35
FIGURE 4.5 Streamwise location of the outer vortex core	36
FIGURE 4.6 Schematic of vortex advection	36

List of Tables

TABLE 2.1 Geometric data of the synthetic jet actuator	11
TABLE 2.2 Synthetic jet operating conditions.....	11
TABLE 3.1 Streamwise locations of the merging points	22
TABLE 3.2 Streamwise locations of the combining points.....	22
TABLE 3.3 Potential core length.....	25

Nomenclature

A	Area
C	Closed curve
CP	Combining point
D	Orifice diameter
D_c	Cavity inner diameter
f	Synthetic jet actuating frequency
H_c	Cavity height
H_o	Orifice plate height
L_o	Stroke length
L_p	Potential core length
MP	Merging point
PIV	Particle image velocimetry
PKE	Phase-correlated kinetic energy
PKE _c	Jet centerline phase-correlated kinetic energy
Re_o	Reynolds number
s	Orifice center distance
t	Time
TKE	Turbulent kinetic energy
U	Time-averaged streamwise velocity
U_o	Synthetic jet characteristic velocity
U_c	Time-averaged jet centerline velocity
U_{max}	Maximum time-averaged streamwise velocity
U_{sym}	Time-averaged symmetry line velocity

$u_o(t)$	Spatial averaged orifice velocity
$u_i(x, t)$	Instantaneous velocity
$U_i(x)$	Time-averaged velocity component
$\tilde{u}_i(x, t)$	phase-correlated velocity component
$u_i'(x, t)$	Fluctuation velocity component
$\langle u_i(x, t) \rangle$	Phase-averaged velocity
u, v	Streamwise and spanwise velocities
x_{mp}	Location of merging point
x_{cp}	Location of combining point
x, y	Streamwise and spanwise coordinate
y'	Coordinate relative to the right jet centerline
$y_{+0.5}$	Outer half-velocity width
Γ	Circulation
Δ	Grid spacing
ν	Kinematic viscosity
τ	Period
φ	Phase
ω_z	Out-of-plane direction vorticity

Chapter 1. Introduction

1.1. Research background

A synthetic jet is a pulsating jet flow including a series of vortices, actuated by an oscillating diaphragm. This device consists of a membrane, cavity and orifice as shown in Figure 1.1. In suction phase, the external fluid is introduced into the cavity, then in the blowing phase it is released through the orifice and forms a propagating vortex ring with a trailing jet. Therefore, synthetic jets have an interesting feature of generating linear momentum flux without net mass flux.

Since synthetic jets have zero net mass flux, the mean velocity of fluid passing through the orifice is zero. Therefore, the characteristic velocity of synthetic jets is defined by stroke length $L_0 = \int_0^{\tau/2} u_o(t) dt$, where $u_o(t)$ is the spatial averaged orifice velocity. This represents the distance which the fluid slug travels during the blowing phase, corresponding to half of the oscillation period τ . Then the characteristic velocity and Reynolds number of the synthetic jet is defined as $U_0 = L_0 f$ and $Re_0 = U_0 D / \nu$ respectively, where f is the operating frequency, D is the orifice diameter, and ν is the fluid kinematic viscosity. The dimensionless stroke length, L_0/D , and Reynolds number are considered the main flow parameters for the synthetic jets.

Synthetic jet behavior and its driving conditions have been widely studied during the last few decades. Comparison of jet properties between synthetic and conventional (continuous) jets has been conducted [1, 2], and it has been shown that synthetic jets have similar velocity profiles to continuous jets, but a larger spreading rate. Holmann *et al.* [3] found the formation criterion of synthetic jets providing required conditions to generate the vortex rings successfully advecting downstream. Other researchers [4–6] reported that the vortex behavior and flow structure of synthetic jets depend on the dimensionless stroke length, but is independent of Reynolds number. Due to the pulsating flow characteristics with large-scale coherent structures, synthetic jet devices have shown good performance in active flow control and heat transfer enhancement. They have been used for lift generation, drag reduction, and separation control of aerodynamic bodies [7, 8], and heat transfer enhancement using synthetic jet impingement has been investigated as an efficient cooling technique [9, 10].

The greater part of flow studies on synthetic jets have been conducted on single jet configurations, but recently, multi-jet configuration is widely adopted in several applications. Segmented synthetic jet devices are commonly used for flow control in wings [8]. Regarding jet impingement cooling, a multi-orifice synthetic jet device configured with a center orifice surrounded by multiple satellite orifices displayed maximum heat transfer coefficient up to

30% higher than that of a single jet [11]. Therefore, flow studies on multiple synthetic jet interaction are necessary and crucial to understand the physical mechanisms for many industrial fields.

1.2. Purpose of research

In the present work, we experimentally study the flow interaction of dual synthetic jets actuated in-phase, emanating from a single cavity, with an emphasis on the dimensionless stroke length. Similar studies were conducted by numerical analysis, but were limited to low Reynolds numbers, and did not examine the effect of the dimensionless stroke length [12, 13]. The pulsating flow from the synthetic jet consists of a vortex ring and trailing jet, and the proportion of the two depends on the dimensionless stroke length, which consequently determines the overall jet characteristics [4, 6, 14]. We assume that the effect of L_0/D is coupled to the spacing s/D between the two jets. Therefore, the flow field measurement is performed for $1.2 \leq s/D \leq 3.0$ and $13.7 \leq L_0/D \leq 28.3$, at fixed $Re_0 = 3700$.

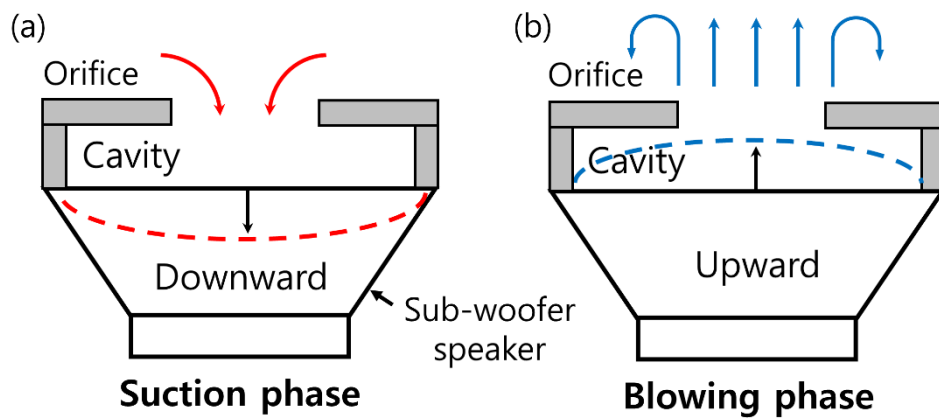


FIGURE 1.1 Working principle of synthetic jet

Chapter 2. Experimental method

2.1. Experimental chamber and dual synthetic jet actuator

The experimental chamber is a cubical acrylic box with each side being 500 mm long. The synthetic jet actuator is attached to the top of the box, and generates synthetic jet flow in the downward direction at the center. Glass windows for providing optical access are attached on the sides of the chamber. The schematic of the experimental setup is shown in Figure 2.1.

The synthetic jet actuator is created by combining a sub-woofer speaker (60W max power, 30W RMS power, frequency response 60–5000Hz) with a circular cylinder-shaped cavity with inner diameter $D_c = 130$ mm and height $H_c = 60$ mm. On the opposite side of the cavity, a replaceable 10 mm thick ($H_o = 10$ mm) acrylic plate with dual circular orifices of 5 mm diameter ($D = 5$ mm) is attached. The spacing between the centers of the two orifices is $s/D = 1.2, 2.0$, and 3.0. The appearance and geometrical data of the actuator are shown in Figure 2.2 and Table 2.1, respectively. The sub-woofer speaker is driven with a sinusoidal voltage signal amplified by an audio amplifier. The wave signal is created from an analog voltage output module. We conducted the experiment under three synthetic jet driving conditions, with the same Reynolds number $Re_\theta = 3700$

and different dimensionless stroke length $L_0/D = 13.7, 19.0$, and 28.3 , as presented in Table 2.2.

2.2. Phase–locked particle image velocimetry

Velocity field measurements of the dual–orifice synthetic jet flow is performed using particle image velocimetry (PIV). A dual–cavity Nd:YAG laser (200 mJ per pulse, wave length of 532 nm) with modular sheet optics is used as the light source. The laser sheet is vertically aligned to pass the centerlines of the two orifices. Digital particle images are obtained by a monotone CCD camera (12 bit depth, 2048×2048 px², 7.4 μm pixel array) with a 105 mm macro lens at $f/2.8$. Tungsten carbide tracer particles with a nominal size of 0.2 μm are used as flow tracers. Particles stored in a seeder are fluidized with compressed air, and the large particles are separated using a cyclone separator, and then seeded into the chamber.

Since the synthetic jet actuator produces periodic fluid motions with high frequency identical to the sinusoidal voltage input to the speaker, a phase–locked PIV system is required to phase–resolve the periodic flow phenomena. The phase–locking of the synthetic jet actuator, laser, and camera is controlled by a custom LabVIEW program and a Timing Hub synchronizer (8 channels, resolution 20 ns). Particle images are acquired at a specific phase at a rate of 10 Hz. Phase resolved measurements are performed at 10–degree intervals from the beginning of the blowing phase, then phase

averaged fields are calculated by averaging 300 instantaneous fields for each phase.

Velocity fields are processed using PIVlab [15], an open source software. For image preprocessing, a high-pass filter, Wiener2 de-noise filter, and contrast-limited adaptive histogram equalization (CLAHE) is applied. The PIV cross-correlation process used a fast Fourier transform (FFT) algorithm using window deformation, and the size of the interrogation area is reduced from 64px with 50% overlap to 32px with the same overlap ratio. A local median test [16] and standard deviation test is then applied to detect velocity vector outliers.

2.3. Data reduction

The instantaneous velocity fields obtained by PIV are decomposed using Reynolds triple decomposition [17], described in Eq. (1),

$$u_i(\mathbf{x}, t) = U_i(\mathbf{x}) + \tilde{u}_i(\mathbf{x}, t) + u_i'(\mathbf{x}, t) \quad (1)$$

where $U_i(\mathbf{x})$ is the time averaged velocity, $\tilde{u}_i(\mathbf{x}, t)$ is the phase-correlated velocity component and $u_i'(\mathbf{x}, t)$ is the velocity fluctuation term. The phase-correlated velocity and the fluctuation velocity are calculated as

$$\tilde{u}_i(\mathbf{x}, t) = \langle u_i(\mathbf{x}, t) \rangle - U_i(\mathbf{x}) \quad (2)$$

$$u'_i(\mathbf{x}, t) = u_i(\mathbf{x}, t) - \langle u_i(\mathbf{x}, t) \rangle \quad (3)$$

where $\langle u_i(\mathbf{x}, t) \rangle$ is the phase averaged velocity. The turbulent kinetic energy (TKE) and the phase-correlated kinetic energy (PKE) which represents the kinetic energy due to the periodic external force [14] are defined as

$$TKE(\mathbf{x}) = \frac{1}{2} \left(\overline{(u'_1)^2} + \overline{(u'_2)^2} \right) \quad (4)$$

$$PKE(\mathbf{x}) = \frac{1}{2} \left(\overline{(\tilde{u}_1^2)} + \overline{(\tilde{u}_2^2)} \right). \quad (5)$$

The out-of-plane direction vorticity is defined as

$$\omega_z = \frac{\partial u}{\partial y} - \frac{\partial v}{\partial x}. \quad (6)$$

Calculating velocity gradients directly using methods such as central differencing amplifies the noise in the PIV data [18], resulting in inaccurate vorticity fields. Therefore, in this study, the circulation-based vorticity calculation method is used:

$$\omega_z = \lim_{A \rightarrow 0} \frac{\Gamma}{A} = \frac{1}{(2\Delta)^2} \oint_C \mathbf{u} \cdot d\mathbf{l}, \quad (7)$$

while Γ is the circulation of an area A , Δ is the grid spacing and C is

the closed curve surrounded by eight neighboring points of each point.

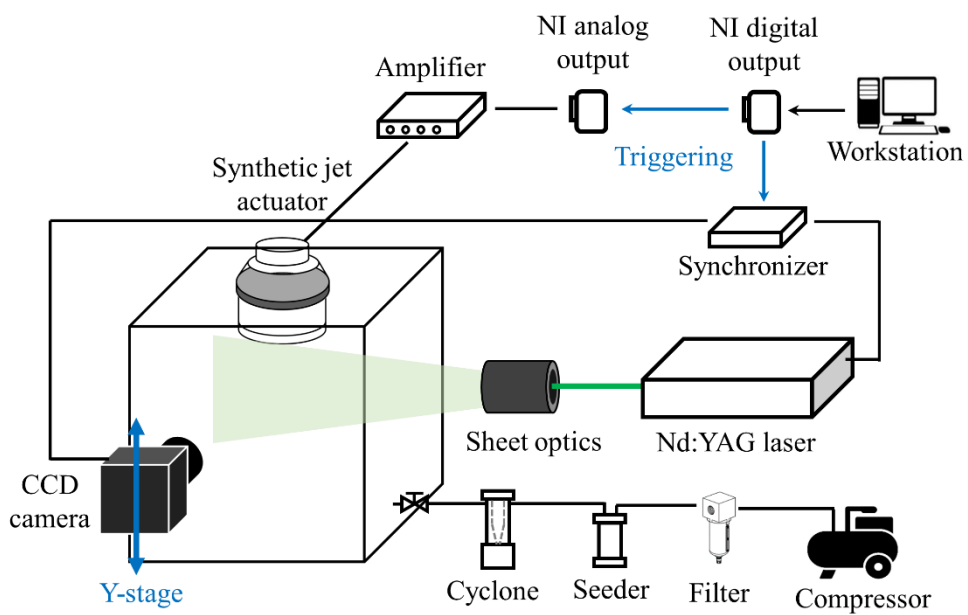


FIGURE 2.1 Experimental setup

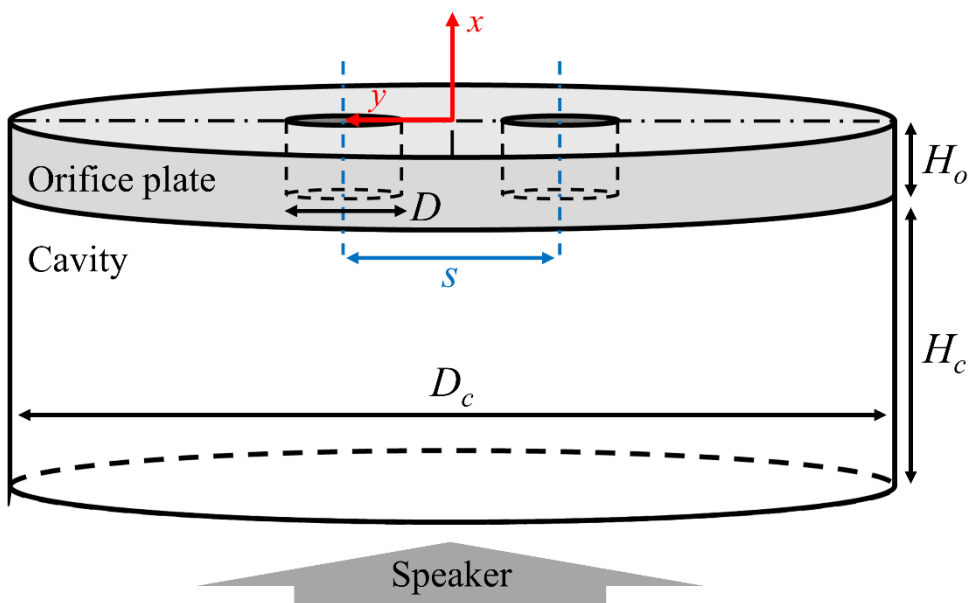


FIGURE 2.2 Dual orifice synthetic jet actuator

Table 2.1 Geometric data of the synthetic jet actuator

Parameter			
Orifice diameter, D [mm]		5	
Orifice plate height, H_o [mm]		10	
Orifice center spacing, s/D	1.2	2.0	3.0
Cavity inner diameter, D_c [mm]		130	
Cavity height, H_c [mm]		60	

Table 2.2 Synthetic jet operating conditions

Condition	Jet 1	Jet 2	Jet 3
Woofer amplification [dB]	18	20	22
Actuation frequency, f [Hz]	160	120	80
Reynolds number, Re_θ		3700	
Dimensionless stroke length, L_θ/D	13.7	19.0	28.3

Chapter 3. Time-averaged flow fields

3.1. Streamwise mean velocity distributions

The twin jet concept used in continuous jet studies is applied in the present study. As shown in Figure 3.1, the flow field is divided into three regions: converging region, merging region, and combined region. At the orifice exit plane ($x = 0$), two individual jets exit, then interact with each other, resulting in the two jet centerlines getting closer. This converging region is concluded at the merging point (x_{mp}), where the value of the symmetry line velocity U_{sym} rises above zero. Further downstream, the two centerlines are completely merged at the combining point (x_{cp}). The region between x_{mp} and x_{cp} is referred as the merging region. After the combining point, the merged jets create a combined jet profile which has a single peak, which is the combined region. Figure 3.2 shows the time-averaged velocity field of one case of a dual synthetic jet measured in the present study. The jet merging and combining are clearly shown, similar to the schematic in Figure 3.1. For dual round synthetic jets, unlike the dual round continuous jets [19], reverse mean flow occurs between the two jet profiles in the converging region, thus forming a recirculation zone. This recirculation zone is likely due to backflow in the suction phase.

Contours of time-averaged streamwise velocity of a fixed dimensionless stroke length $L_0/D = 28.3$ for various orifice spacing

$s/D = 1.2, 2.0,$ and 3.0 are displayed in Figure 3.3. The velocity profiles of two jets are separately formed initially, then spread outward freely and inward to the symmetry plane ($y = 0$). The growth of the inner shear layers of the two jets is confined, unlike the outer shear layers. A cone shape recirculation region is developed between the inner layers, then terminates at the merging point where the inner layers grow and eventually merge. As the orifice spacing decreases the jet interaction becomes stronger, resulting in the earlier merging of the two jets, and a shorter converging region. Figure 3.4 shows the contours of time-averaged streamwise velocity of a fixed orifice spacing $s/D = 3.0$ for various dimensionless stroke length $L_o/D = 13.7, 19.0,$ and 28.3 . The difference in the jet merging is not shown clearly, but we can see that the jet core is developed longer as L_o/D increases. This is because the trailing jet of each single jet is enhanced as the L_o/D increases for the same Re_o [4, 14].

Figure 3.5 shows the normalized streamwise velocities along the jet centerline and the symmetry line. The jet centerline velocity U_c has lower value near the orifice plane due to the zero-net-mass-flux property of the synthetic jet, then reaches maximum velocity at $x/D = 1.5 - 2.0$ downstream. On the other hand, the symmetry line velocity U_{sym} has negative value near the orifice, then increases to positive value at merging point. This recirculating flow is due to the backflow into the orifice in the suction phase of the synthetic jet

driving cycle. As s/D increases the jet interaction is weakened, therefore, the magnitude of U_{sym} in the recirculation region becomes smaller and the distance to the merging point increases (Figure 3.5a). The jet centerline velocity U_c tends to decay slightly more rapidly as s/D is reduced, as the entrainment is enhanced due to the stronger jet interaction. The U_c and U_{sym} finally merges at the combining point further downstream, then gradually decay. The combining point is also farther downstream as s/D increases. Figure 3.5b shows the three different L_o/D jets for the jet configuration $s/D = 3.0$. A decrease in L_o/D for the same Reynolds number increases the effect of the vortex ring rather than the trailing jet [4, 14]. The vortex ring enhances the entrainment and jet interaction, which leads to rapid increase in U_{sym} and slight decrease in U_c . Consequently, the combining occurs earlier as L_o/D decreases.

The merging point x_{mp} , the end of the recirculating region between the jets, is defined as the streamwise location where U_{sym} equals to zero. The combining point is defined as the point where the symmetry line and the centerline merges, thus x_{cp} is determined as the location where the U_{sym} and U_c become nearly identical, $U_{sym}/U_c = 0.99$ in this study. The x_{mp} and x_{cp} of all cases are shown in Table 3.1 and Table 3.2, respectively. Figure 3.6a shows the tendency of x_{mp} and x_{cp} for various s/D and L_o/D . Both distances similarly increase as the orifice separation increases, but only x_{cp} is affected by L_o/D . This implies the growth of the merging region, defined as $x_{cp} - x_{mp}$,

with increment in L_0/D . As shown in Figure 3.6b, the merging region extends linearly with the dimensionless stroke length.

The normalized profiles of the time-averaged streamwise velocity are displayed in Figure 3.7. The profiles are obtained at streamwise locations after the end of the potential core and until the combining point. Potential core length L_p is shown in Table 3.3, which is determined by the location where $U_c = 0.9U_{max}$ as in conventional jet studies. L_p tends to increase as s/D and L_0/D increases. The former tendency is due to less jet interaction as s/D increases, causing the shear layers to merge later. The latter is because the influence of the trailing jet becomes larger as L_0/D increases, which make the synthetic jets act like continuous jets [14]. The time-averaged streamwise velocity in Figure 3.7 is normalized by the right jet centerline velocity. The coordinate y' is a coordinate relative to the right jet centerline and is normalized by the outer half-velocity width $y_{+0.5}$ (Figure 3.8). The outer profiles ($y' > 0$) show good self-similarity, while the inner profiles ($y' < 0$) become wider downstream due to the jet interaction.

3.2. TKE and PKE contours

Contours of turbulent kinetic energy (TKE) of a fixed $s/D = 3.0$ for various $L_0/D = 13.7, 19.0, 28.3$ are shown in Figure 3.9. For each single jet, a potential core region of lower TKE and outer and inner shear layers of higher TKE are shown. The outer shear layer is more

developed than the inner shear layer, because the jet can freely spread outward, but is confined inward by the other jet. As L_0/D increases, the proportion of the trailing jet is increased compared to that of the vortex ring. Therefore, the shear layers of each jet which are related to the trailing jet become stronger, and the TKE in the region between the two jets (near the symmetry line) becomes weaker.

Contours of the phase-correlated kinetic energy (PKE) of a fixed $s/D = 3.0$ for various $L_0/D = 13.7, 19.0, 28.3$ are shown in Figure 3.10. The PKE represents the kinetic energy caused by the periodic external force. Therefore, the maximum PKE value appears at the orifice exit, and then monotonically decreases both in the streamwise direction along the jet centerline and the spanwise direction from the centerline. The overall PKE value becomes higher as L_0/D increases due to the higher amplitude of the sub-woofer speaker (Table 2.2). In addition, a self-similar behavior is observed for the normalized PKE profile in the y' coordinate (Figure 3.11). Similar to the streamwise velocity profile, the inner profile becomes wider than the outer one downstream. And the outer PKE profile shows a narrower curve than that of the velocity profile, as reported in a single round synthetic jet study [14].

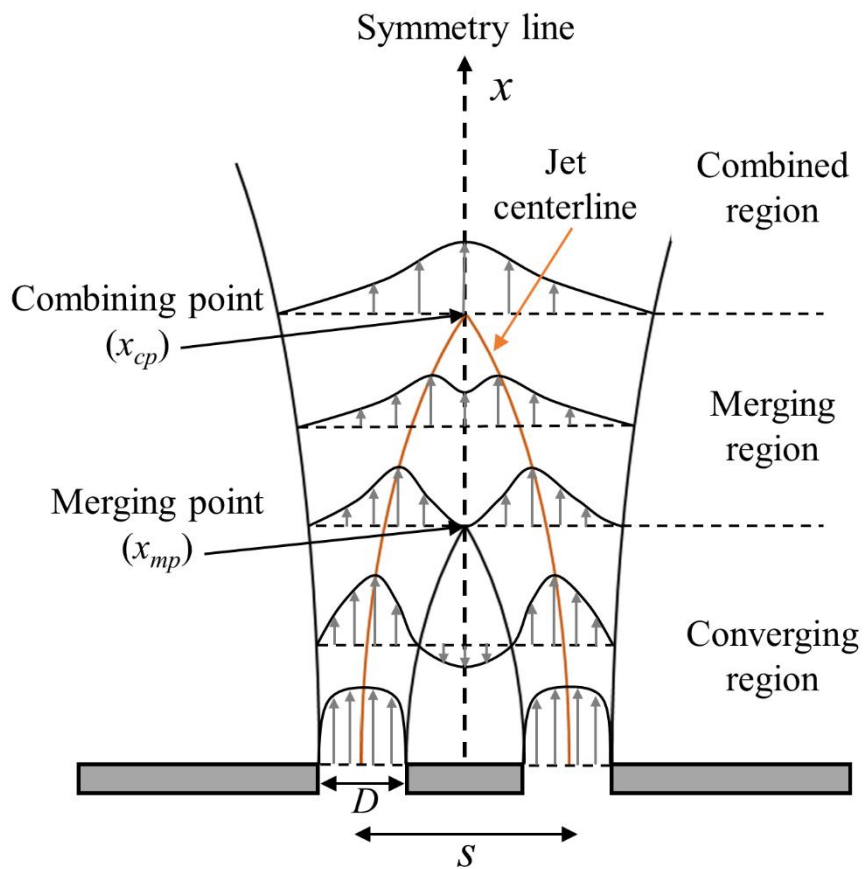


FIGURE 3.1 Schematic of dual jet configuration

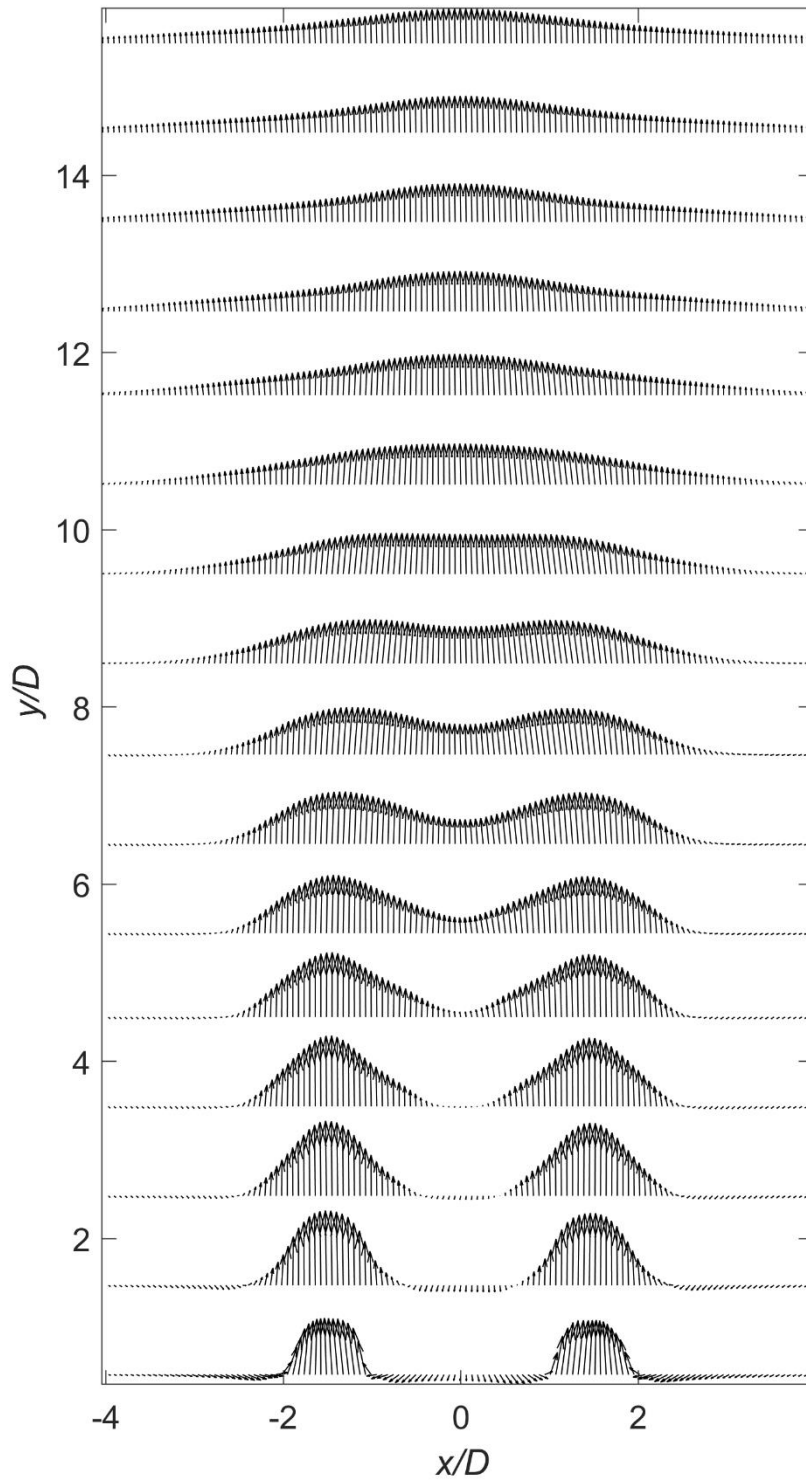


FIGURE 3.2 Example of dual synthetic jet flow field ($s/D = 3.0$ & $L_0/D = 28.3$)

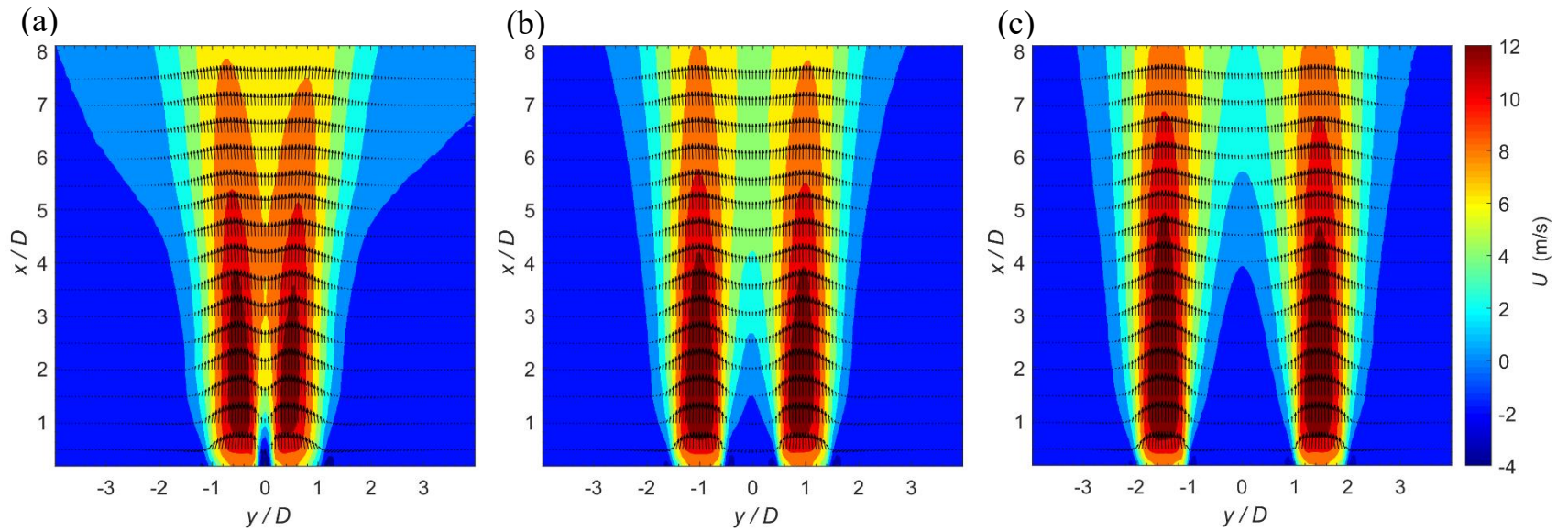


FIGURE 3.3 Time-averaged streamwise velocity contours with dimensionless stroke length $L_0/D = 28.3$, for (a) $s/D = 1.2$, (b) $s/D = 2.0$, and (c) $s/D = 3.0$.

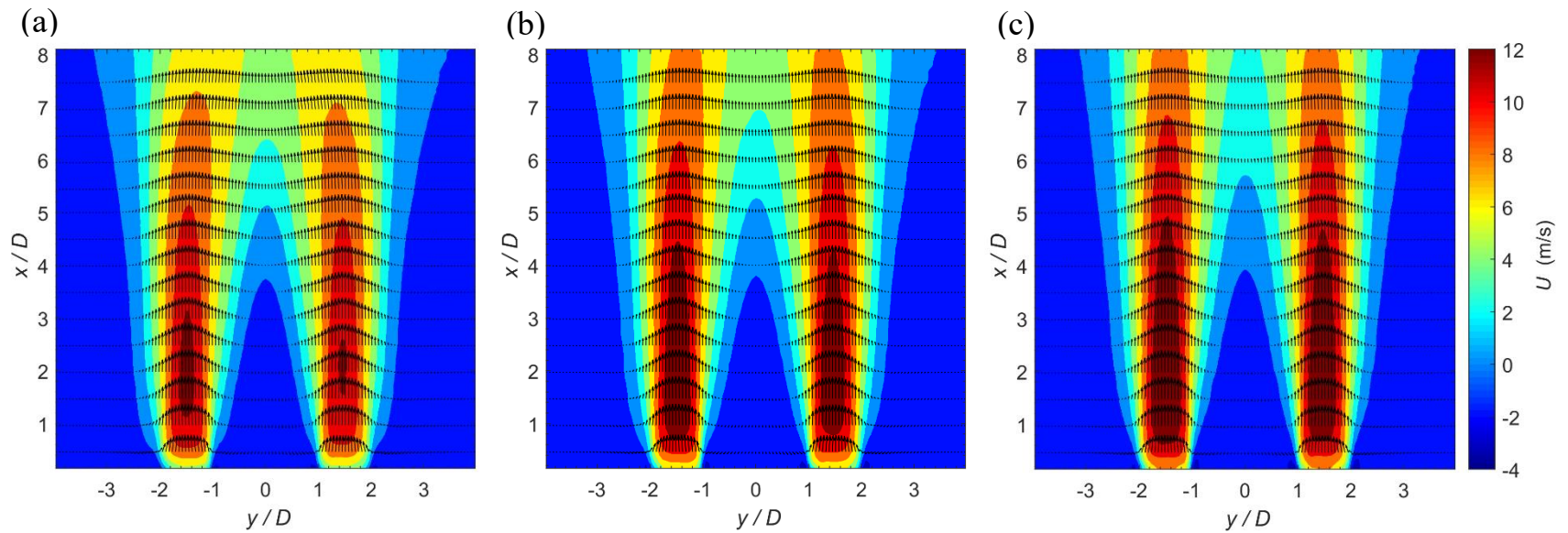


FIGURE 3.4 Time-averaged streamwise velocity contours with orifice spacing $s/D = 3.0$, for (a) $L_o/D = 13.7$, (b) $L_o/D = 19.0$, and (c) $L_o/D = 28.3$.

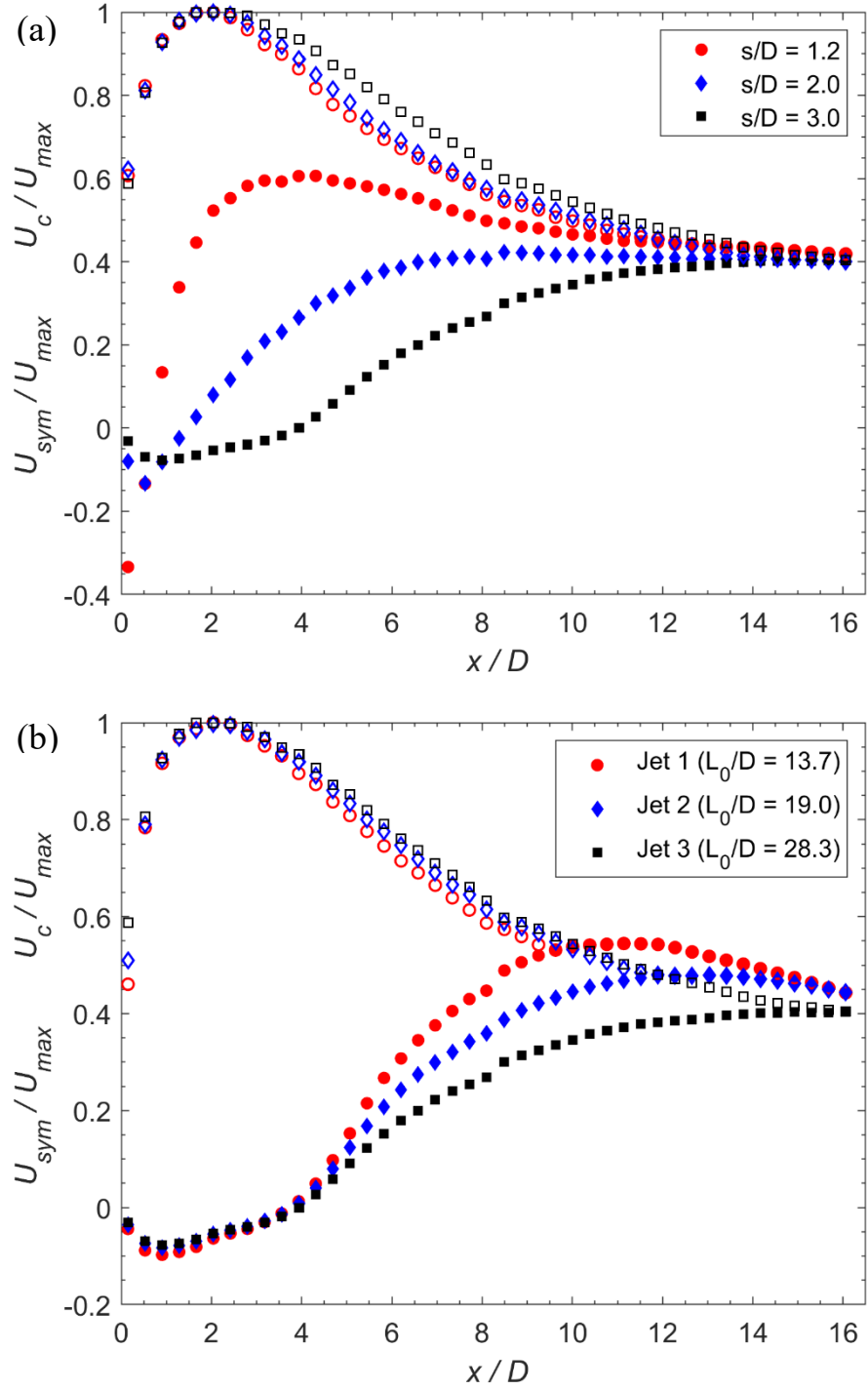


FIGURE 3.5 Normalized streamwise velocities along the centerline (unfilled marker) and symmetry line (filled marker), for (a) fixed $L_0/D = 28.3$, and (b) fixed $s/D = 3.0$.

Table 3.1 Streamwise locations of the merging points

Merging point: x_{mp}/D			
	$L_0/D = 13.7$	$L_0/D = 19.0$	$L_0/D = 28.3$
$s/D = 1.2$	0.57	0.66	0.72
$s/D = 2.0$	1.03	1.22	1.49
$s/D = 3.0$	3.74	3.81	3.93

Table 3.2 Streamwise locations of the combining points

Combining point: x_{cp}/D			
	$L_0/D = 13.7$	$L_0/D = 19.0$	$L_0/D = 28.3$
$s/D = 1.2$	6.62	9.52	12.38
$s/D = 2.0$	7.02	10.22	14.30
$s/D = 3.0$	9.45	11.85	15.78

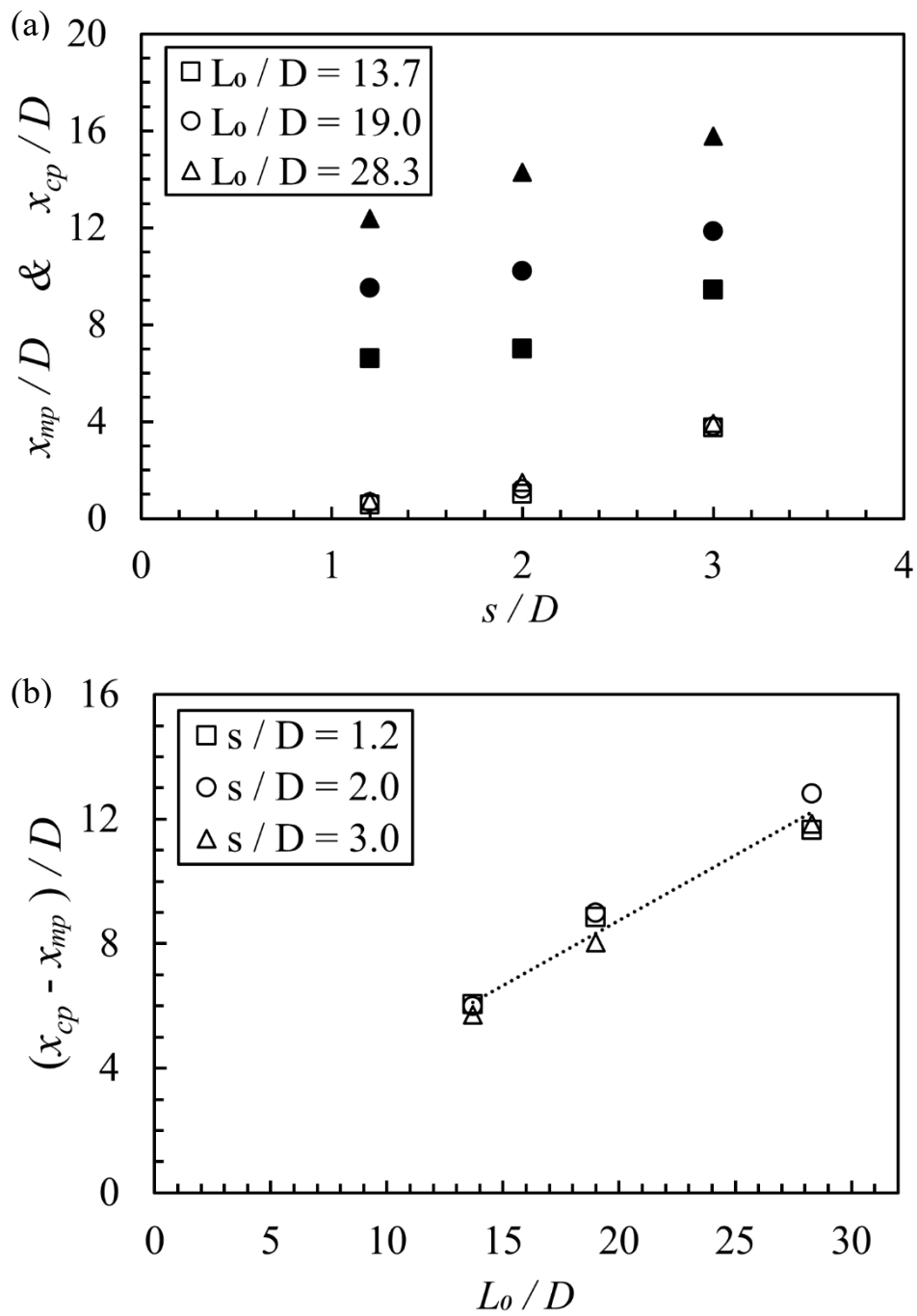


FIGURE 3.6 (a) Streamwise locations of the merging points (unfilled marker) and the combining points (filled marker).
(b) Extent of the merging region

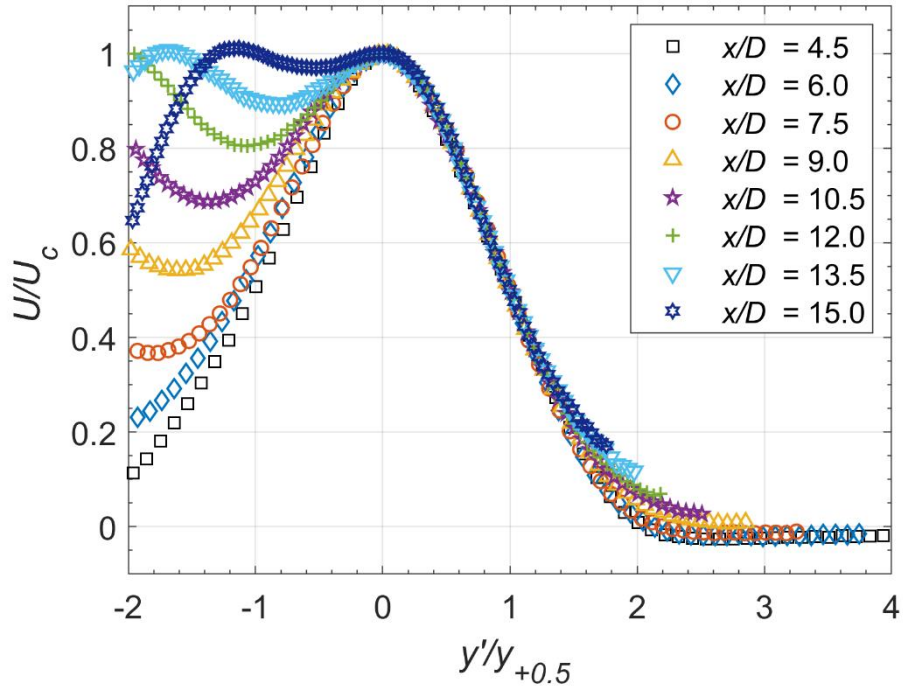


FIGURE 3.7 Normalized streamwise velocity profiles in the region of $L_p < x < x_{cp}$, for $s/D = 3.0$ & $L_0/D = 28.3$.

Table 3.3 Potential core length

Potential core length: L_p/D			
	$L_0/D = 13.7$	$L_0/D = 19.0$	$L_0/D = 28.3$
$s/D = 1.2$	2.75	3.16	3.54
$s/D = 2.0$	2.95	3.35	3.79
$s/D = 3.0$	3.88	4.23	4.38

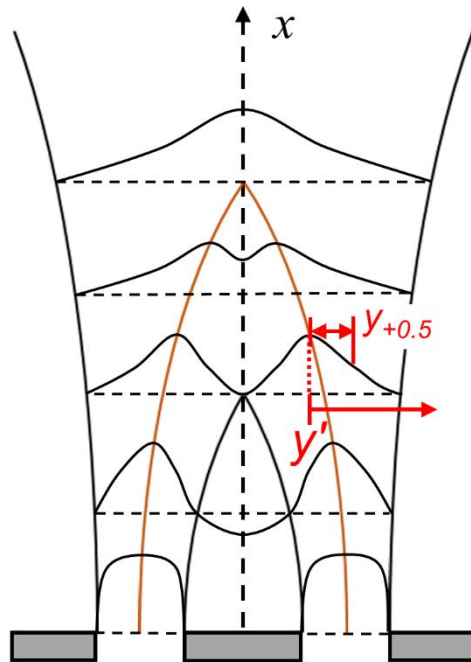


FIGURE 3.8 Outer half-velocity width and y' coordinate

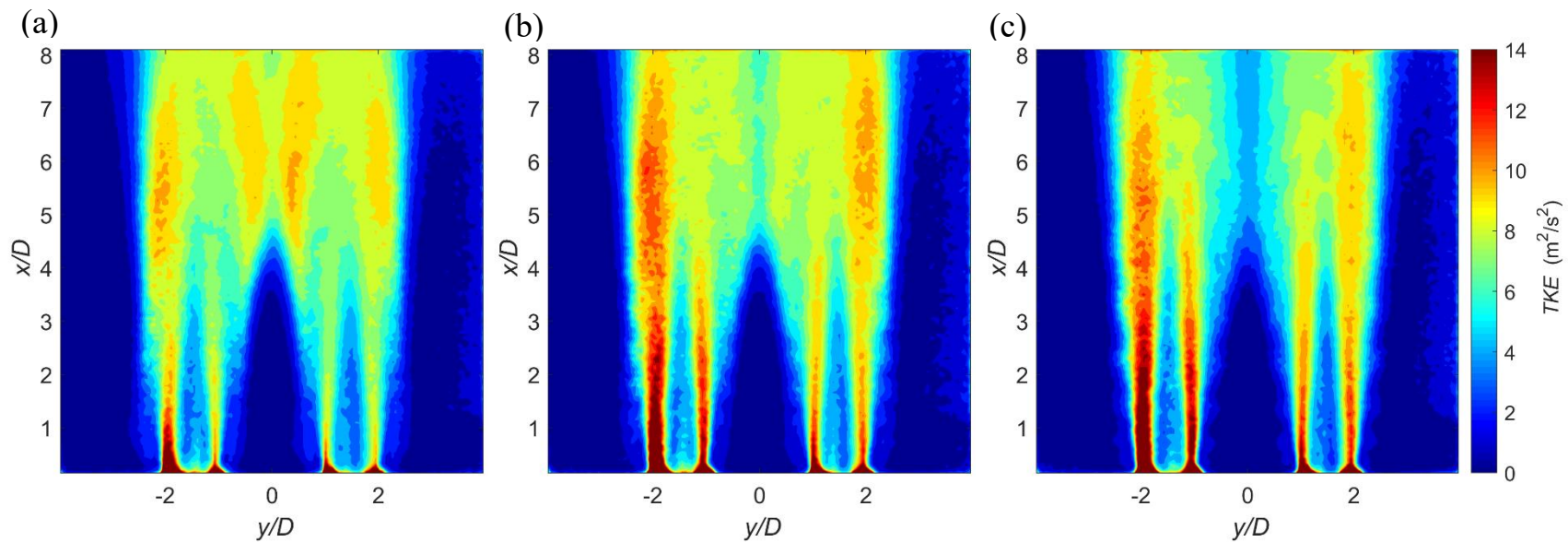


FIGURE 3.9 Contours of turbulent kinetic energy (TKE) with the orifice spacing $s/D = 3.0$, for (a) $L_o/D = 13.7$, (b) $L_o/D = 19.0$, and (c) $L_o/D = 28.3$.

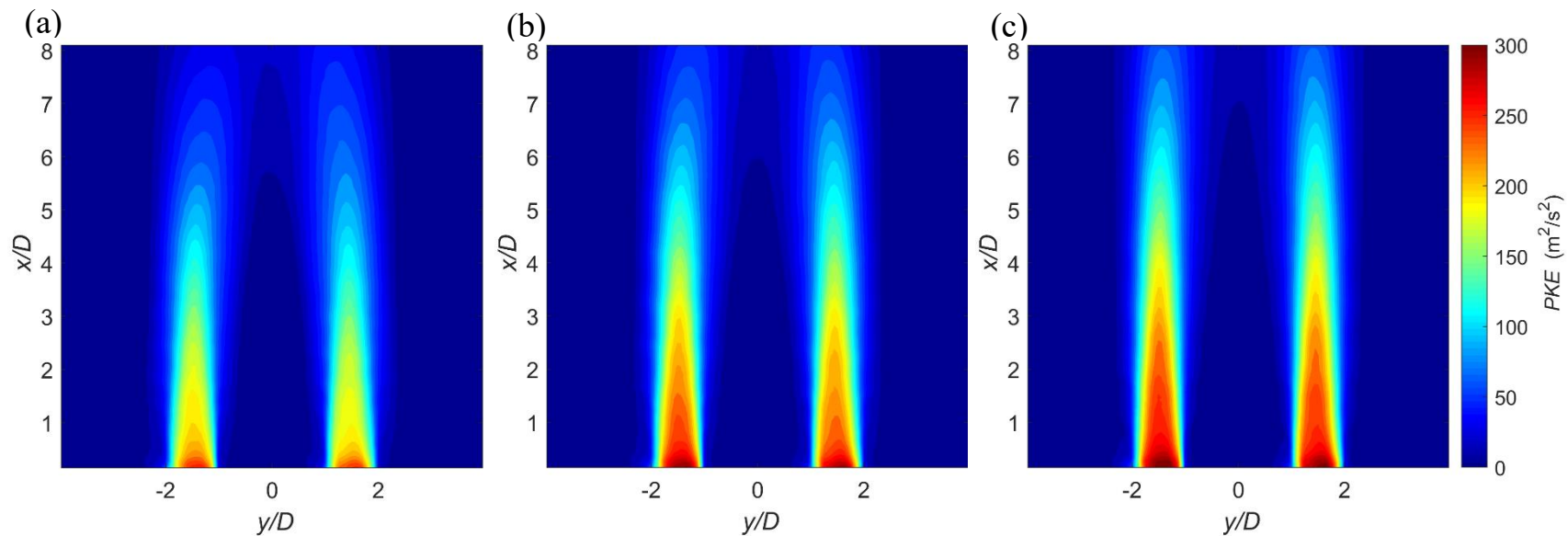


FIGURE 3.10 Contours of phase-correlated kinetic energy (PKE) with the orifice spacing $s/D = 3.0$, for (a) $L_o/D = 13.7$, (b) $L_o/D = 19.0$, and (c) $L_o/D = 28.3$

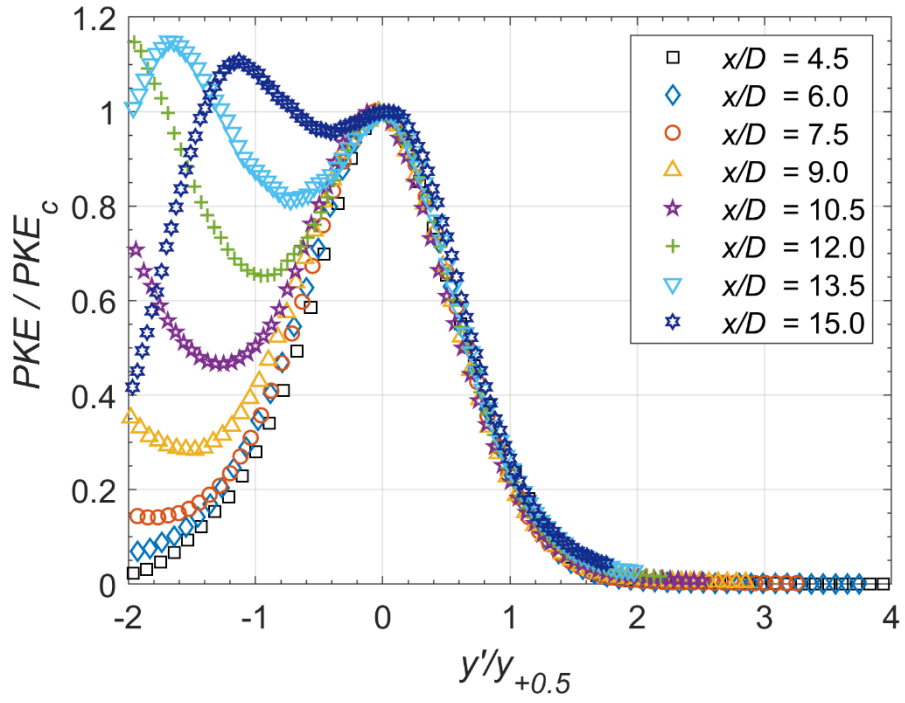


FIGURE 3.11 Normalized PKE profiles in the region of $L_p < x < x_{cp}$, for $s/D = 3.0$ & $L_0/D = 28.3$.

Chapter 4. Phase-averaged flow fields

4.1. Phase-averaged vorticity contours

The time-averaged jet-like behavior of the synthetic jet results from its pulsating flow consisting of advecting vortex rings and trailing jet. Therefore, phase-resolved flow analysis is performed to understand the evolution of the synthetic jet flow.

Figure 4.1 shows the phase-averaged vorticity fields for $s/D = 3.0$ and $L_0/D = 13.7$. Only the right jet is displayed since the flow fields are symmetric with respect to the x -axis. The initial phase $\phi = 0^\circ$ is the moment that the blowing phase begins. At the early blowing phase (Figure 4.1a-c), the outer vortex (negative vorticity due to clockwise rotation) and the inner vortex (positive vorticity due to counter-clockwise rotation) are ejected almost symmetrically. After the primary ejection phase, the leading vortex pair and the shear layer of the trailing jet is clearly observed, and the inner vortex stretches in the x direction (Figure 4.1d-f). After that the inner vortex interacts with the opposite symmetric jet and starts to cancel out (Figure 4.1g-h), and part of the inner vortex jumps ahead of the outer vortex, and dissipates outward (Figure 4.1i-l). The remnant vortex, which is called the merged vortex pair, advects downstream with its self-induced velocity.

The phase-averaged vorticity fields of the smallest $s/D = 1.2$ and the same $L_0/D = 13.7$ are displayed in Figure 4.2. Since the

orifice spacing is shorter than the $s/D = 3.0$ case (Figure 4.1), the jet interaction is stronger, and the vortex pair is asymmetric, such that the inner vortex is not as well developed as the outer vortex (Figure 4.2a–c). Furthermore, the deformation and cancellation of the inner vortex occur (Figure 4.2d–e) at an earlier phase and closer location to the orifice than the former case.

Figure 4.3 depicts the phase-averaged vorticity fields for $s/D = 1.2$, and the largest $L_o/D = 28.3$. The overall vortex advection becomes much faster than the case of $L_o/D = 13.7$ (Figure 4.2). Thus, the generation of vortices and interaction of inner vortex occur at much earlier phases (Figure 4.3a–f). However, the flow structures during the vortex interactions such as generation, deformation, and cancellation are similar. This feature is more obvious in Figure 4.4, which shows snapshots at the phases of similar flow structures, for $s/D = 1.2$ and three different L_o/D cases. For each L_o/D case, three snapshots are captured right after the vortex pair generation, inner vortex deformation, and jumping ahead of the outer vortex, respectively. As L_o/D increases, the flow structures at each moment are similar, and only the phase is advanced because of the faster vortex advection.

4.2. Vortex advection

The location of the outer vortex core during the actuation cycle is plotted in Figure 4.5. The vortex core is defined as a point of

maximum phase-averaged vorticity in each phase. The vorticity fields are filtered by a box filter size of 7 to improve the identification of the vortices in the far field where the vortices are dissipated. In the beginning of the cycle, the vortex is generated, and its advection is accelerated. After the vortices merge, which corresponds to the cancellation of the inner vortex, the merged vortex advects downstream at a slower constant speed. This tendency is described in Figure 4.6.

As s/D increases for fixed L_0/D , the confinement and interaction of the inner vortex is weakened, resulting in delayed vortex merging. The advection speed of the vortex does not seem to vary, since it is determined mainly by L_0/D . As L_0/D increases for fixed s/D , the vortex advection speed increases during the entire cycle, as evidenced by the increased slope of the curves (Figure 4.5).

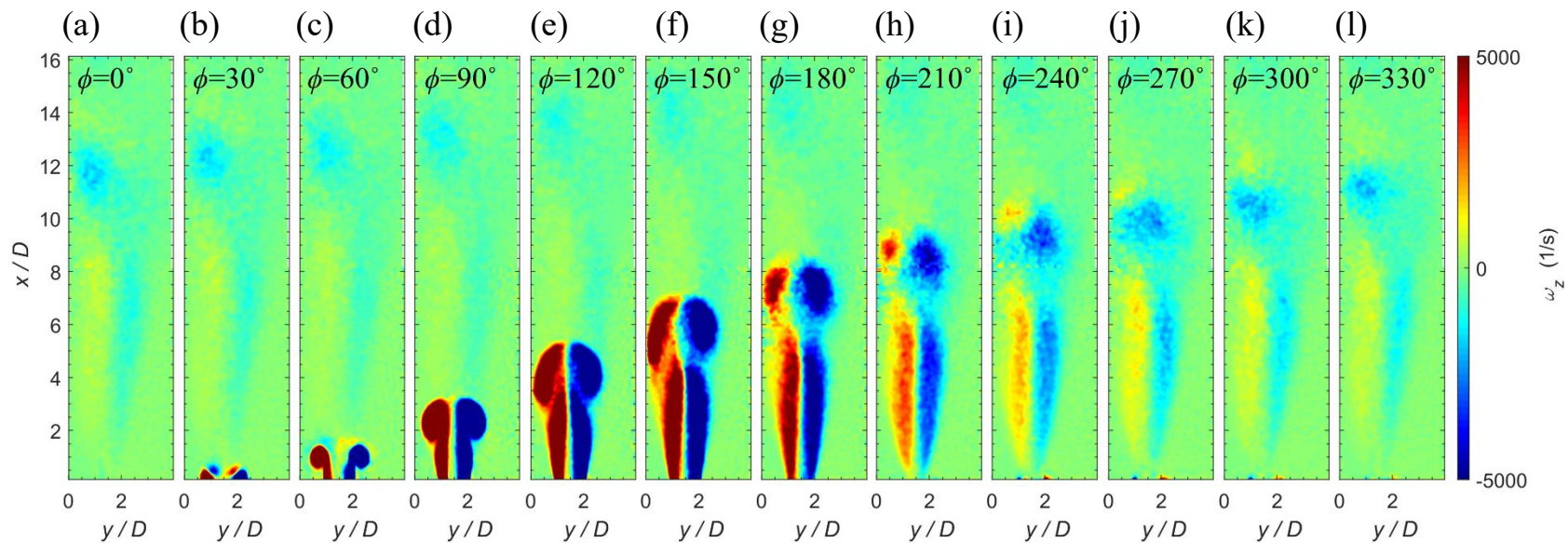


FIGURE 4.1 Phase-averaged vorticity contours for $s/D = 3.0$ and $L_0/D = 13.7$

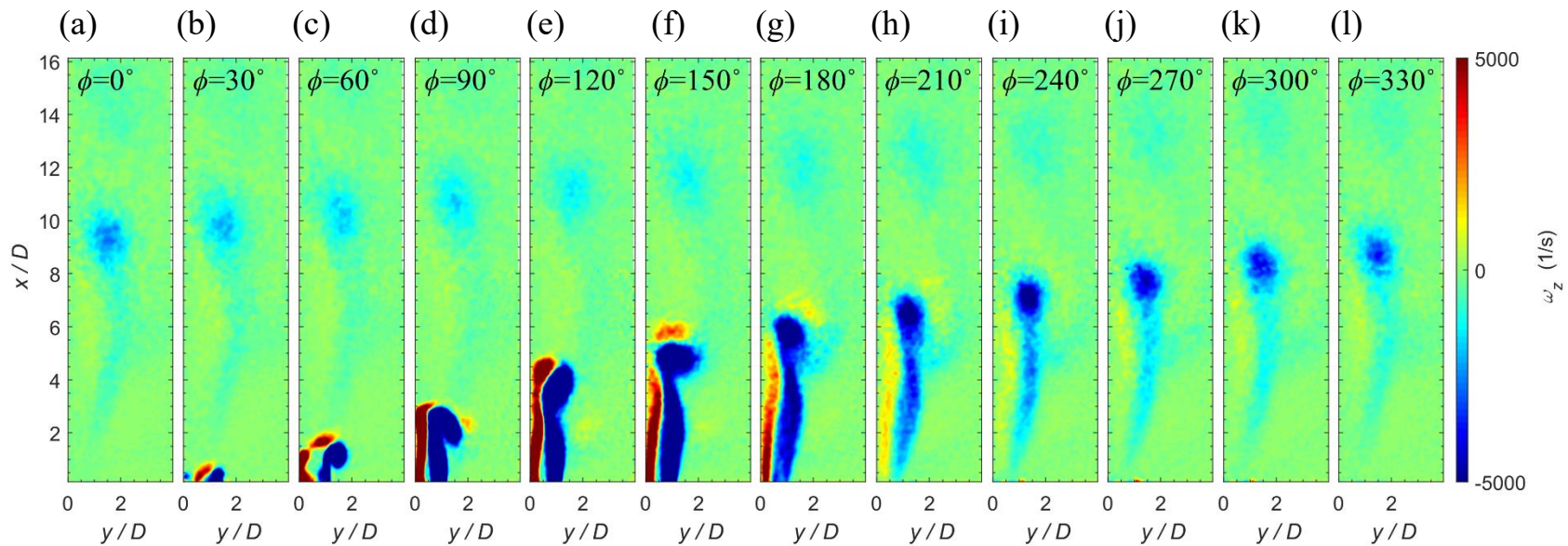


FIGURE 4.2 Phase-averaged vorticity contours for $s/D = 1.2$ and $L_0/D = 13.7$

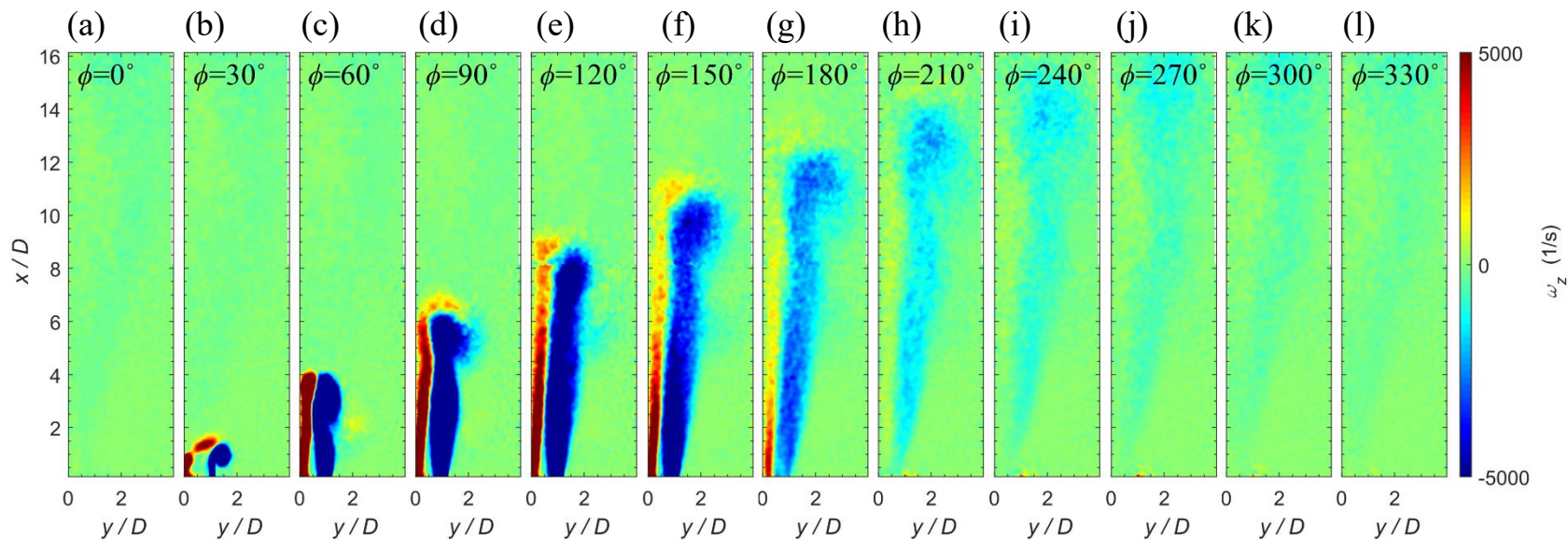


FIGURE 4.3 Phase-averaged vorticity contours for $s/D = 1.2$ and $L_0/D = 28.3$

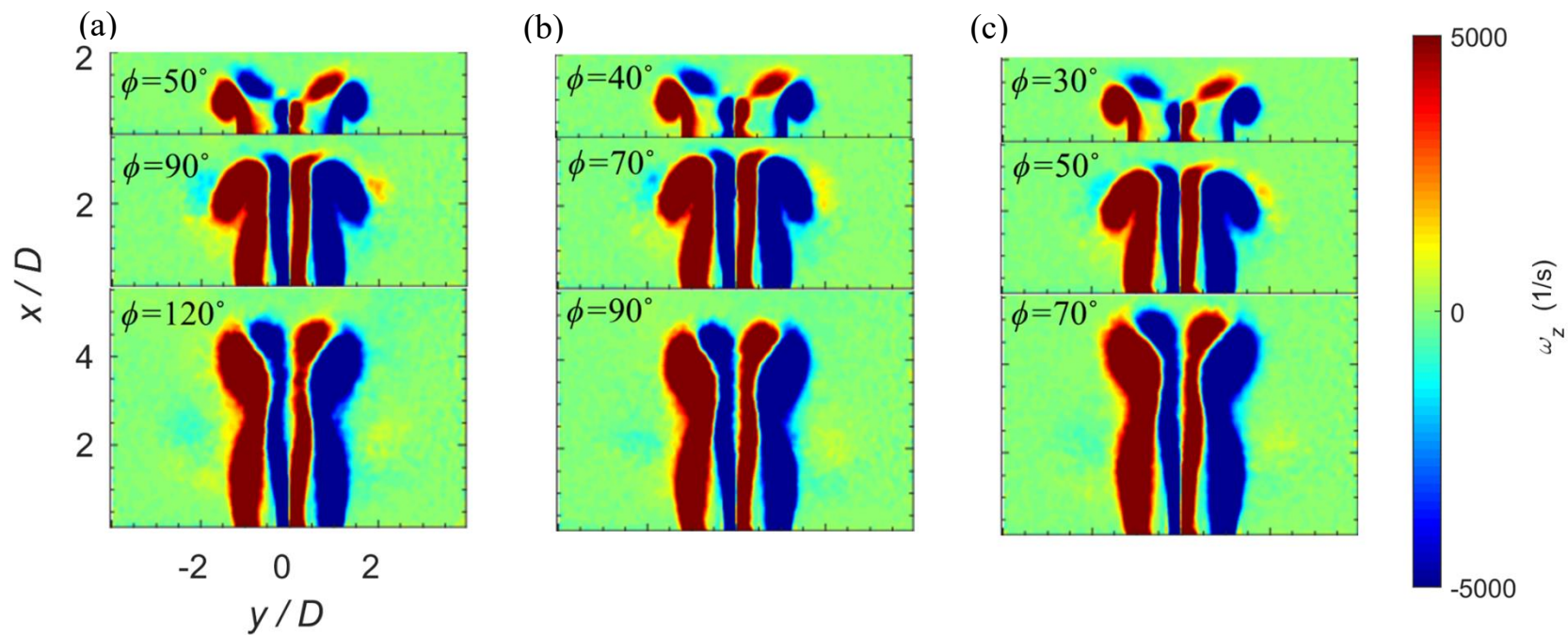


FIGURE 4.4 Snapshots of phase-averaged vorticity contours of $s/D = 1.2$, for (a) $L_o/D = 13.7$, (b) $L_o/D = 19.0$, and (c) $L_o/D = 28.3$

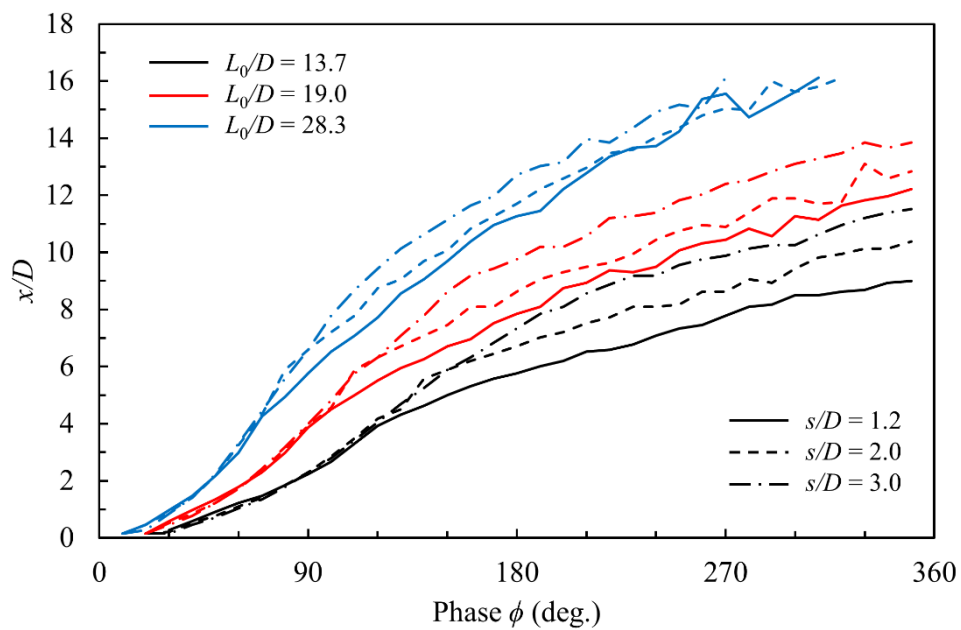


FIGURE 4.5 Streamwise location of the outer vortex core

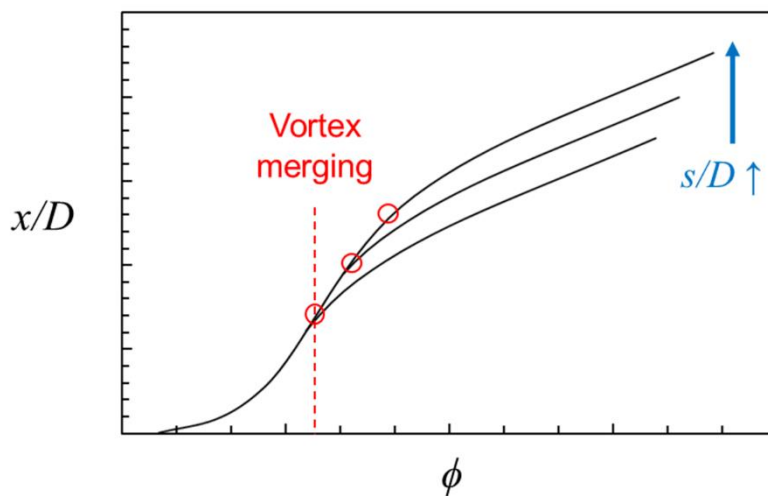


FIGURE 4.6 Schematic of vortex advection

Chapter 5. Conclusion

An experimental study on the flow interaction of two synthetic jets generated by a dual-orifice actuator is conducted by phase-locked PIV. Dual synthetic jets are actuated at a fixed Reynolds number of 3700, for three different orifice spacings $s/D = 1.2, 2.0$, and 3.0 , and dimensionless stroke lengths $L_0/D = 13.7, 19.0$, and 28.3 . The effects of the orifice spacing and the dimensionless stroke length on the time- and phase-averaged flow fields are investigated.

As the orifice spacing decreases, the interaction between the two jets are enhanced, resulting in rapid decay of the jet centerline velocity and increase of the symmetry line velocity, thus causing earlier jet merging and combining. As the dimensionless stroke length increases, the effect of the trailing jet is enhanced and the effect of the vortex ring is decreased, which leads to weaker entrainment and jet interaction. The locations of the merging point and combined point tend to increase as the orifice spacing increases, and the merging region shows linear growth with increase of the dimensionless stroke length. Consequently, the overall jet merging and combining is enhanced as the orifice spacing and the dimensionless stroke length decrease.

Utilizing phase-averaged measurements, the periodic behavior of the vortex and trailing jet can be observed. Inner and outer vortices are generated right after the blowing begins. Shortly

thereafter, the inner vortices interact with each other, and result in deformation and cancellation. After that, the remaining inner vortex jumps ahead of the outer vortex and dissipates outward, and only the merged vortex pair remains and advects downstream. A decrease of the orifice spacing restrains the generation and enhances the interaction of the inner vortex, resulting in earlier vortex merging. Meanwhile, the increase of dimensionless stroke length only increases the speed of vortex advection, while the interacting flow structures remain similar.

Bibliography

1. Cater, J.E. and J. Soria, *The evolution of round zero-net-mass-flux jets*. Journal of Fluid Mechanics, 2002. **472**: p. 167–200.
2. Smith, B. and G. Swift, *A comparison between synthetic jets and continuous jets*. Experiments in Fluids, 2003. **34**(4): p. 467–472.
3. Holman, R., et al., *Formation criterion for synthetic jets*. AIAA Journal, 2005. **43**(10): p. 2110–2116.
4. Shuster, J.M. and D.R. Smith, *Experimental study of the formation and scaling of a round synthetic jet*. Physics of Fluids, 2007. **19**(4): p. 045109.
5. Valiorgue, P., et al., *Heat transfer mechanisms in an impinging synthetic jet for a small jet-to-surface spacing*. Experimental Thermal and Fluid Science, 2009. **33**(4): p. 597–603.
6. McGuinn, A., et al., *Flow regime characterisation of an impinging axisymmetric synthetic jet*. Experimental Thermal and Fluid Science, 2013. **47**: p. 241–251.
7. Amitay, M. and A. Glezer, *Aerodynamic flow control using synthetic jet actuators*, in *Control of Fluid Flow*. 2006, Springer. p. 45–73.
8. Gilarranz, J., L. Traub, and O. Rediniotis, *A new class of synthetic jet actuators—part II: application to flow separation control*. Journal of Fluids Engineering, 2005. **127**(2): p. 377–387.
9. Pavlova, A. and M. Amitay, *Electronic cooling using synthetic jet impingement*. Journal of Heat Transfer, 2006. **128**(9): p. 897–907.
10. Chaudhari, M., B. Puranik, and A. Agrawal, *Heat transfer characteristics of synthetic jet impingement cooling*. International Journal of Heat and Mass Transfer, 2010. **53**(5–6): p. 1057–1069.

11. Chaudhari, M., B. Puranik, and A. Agrawal, *Multiple orifice synthetic jet for improvement in impingement heat transfer*. International Journal of Heat and Mass Transfer, 2011. **54**(9–10): p. 2056–2065.
12. Riazi, H. and N. Ahmed. *Numerical investigation on two-orifice synthetic jet actuators of varying orifice spacing and diameter*. in *29th AIAA Applied Aerodynamics Conference*. 2011.
13. Palumbo, A., et al. *Numerical study on the flow field generated by a double-orifice synthetic jet device*. in *Proceedings of the 24rd Conference of the Italian Association of Theoretical and Applied Mechanics*. 2019.
14. Greco, C.S., G. Cardone, and J. Soria, *On the behaviour of impinging zero-net-mass-flux jets*. Journal of Fluid Mechanics, 2017. **810**: p. 25–59.
15. Thielicke, W. and E. Stamhuis, *PIVlab-towards user-friendly, affordable and accurate digital particle image velocimetry in MATLAB*. Journal of Open Research Software, 2014. **2**(1).
16. Westerweel, J. and F. Scarano, *Universal outlier detection for PIV data*. Experiments in Fluids, 2005. **39**(6): p. 1096–1100.
17. Hussain, A.K.M.F. and W.C. Reynolds, *The mechanics of an organized wave in turbulent shear flow*. Journal of Fluid Mechanics, 1970. **41**(2): p. 241–258.
18. Westerweel, J., *Digital particle image velocimetry-theory and application*. 1993, Delft University of Technology: The Netherlands.
19. Laban, A., et al., *Experimental investigation of nozzle spacing effects on characteristics of round twin free jets*. Journal of Fluids Engineering, 2019. **141**(7): p. 071201.

요약

합성 제트 장치는 내부의 작동 유체를 오리피스를 통해 내보내면서 와류 고리를 포함한 펄스 제트를 생성한다. 이는 총 질량 변화 없이 모멘텀을 발생시킬 수 있어 유체 공급을 위한 파이프 등이 불필요하며, 연속 제트에 비해 높은 확산율을 가지기 때문에 능동 유동 제어와 제트 충돌 냉각 등 다양한 응용분야에 쓰이고 있다. 최근에는 다중 합성 제트를 사용해 모멘텀 생성과 혼합을 증대시킴으로써 응용분야에서의 효율이 향상됨이 보고되고 있다. 따라서 본 연구에서는 두 합성제트 간 유동 상호작용 연구를 통해 합성 제트의 응용 가능성을 극대화하고자 한다. 실험 유동은 듀얼 오리피스 - 단일 공동 합성 제트에서 생성하였으며, 고정된 레이놀즈 수 조건에서 다양한 제트간 거리와 무차원화된 스트로크 길이에 대해 수행했다. 평균 유동장과 위상 분해 유동장의 측정은 위상 동기 PIV를 사용해 수행되었다. 제트간 거리가 감소하고 무차원화된 스트로크 길이가 감소함에 따라 두 합성제트간 상호작용이 증대되면서, 시간 평균 된 제트 중심속도의 빠른 감소와 확산이 발생하였다. 동시에 오리피스 사이 대칭축 상의 유속이 빠르게 증가하여 두 제트의 접촉 위치와 결합 위치가 가까워짐이 관찰되었다. 구동 주기 동안 오리피스에서 방출된 내부의 와류는 서로 상호작용하면서 유동방향으로의 변형을 거쳐 대부분 상쇄되며 이윽고 외부의 와류를 주월하면서 소산하였고, 남아있는 각 제트의 외부 와류는 새로운 와류 쌍을 형성하여 진행함이 관찰되었다. 와류간 상호작용은 제트간 거리가 가까워짐에 따라 더 이른 시점에 오리피스 가까이에서 발생하였으며, 스트로크 길이가 증가함에 따라 와류 상호작용의 유동 형태는 변하지 않았으나, 강화된 후행 제트의 영향으로 전체적인 거동이 빠르게 진행됨을 보였다.

주요어: 합성 제트, 이중 제트, 제트 간 상호작용, 위상 동기 PIV, 와류
학번: 2018-29172